DIRECT PUFFING SIMULATION OF MISCIBLE AND EMULSIFIED MULTICOMPONENT SINGLE DROPLETS*

J. Huang,[1] J. Xia,[2,*] Y. He,[1] Z.H. Wang,[1] & K.F. Cen[1]

[1]*State Key Laboratory of Clean Energy Utilization, Zhejiang University, Hangzhou 310027, China*

[2]*Department of Mechanical and Aerospace Engineering & Institute of Energy Futures, Brunel University London, Uxbridge UB8 3PH, UK*

*Address all correspondence to: J. Xia, Department of Mechanical and Aerospace Engineering & Institute of Energy Futures, Brunel University London, Uxbridge UB8 3PH, UK, E-mail: jun.xia@brunel.ac.uk

Original Manuscript Submitted: 11/15/2023; Final Draft Received: 04/26/2024

The aim of the present study is to achieve direct simulation of the puffing of a multicomponent droplet using interface capturing approaches. A non-ideal multicomponent phase equilibrium model is used to determine the composition of boiled vapour. Firstly, the puffing of a two-miscible-component (ethanol:water=1:1 in wt.%) droplet in two-dimensional configuration is directly simulated. The distribution of ejected vapour is impacted by a rotating and shape oscillating satellite droplet. The ejected vapour contains much more ethanol than water, facilitating the transport of the volatile fuel component inside the droplet to the ambient air. The morphological changes to the droplet induced by puffing promote considerably the contact of the boiling surface with air, significantly increasing the scalar dissipation rate of vapour/air. The effects of the nucleation bubble location and droplet temperature on puffing were investigated. Secondly, the puffing of an emulsified three-component (ethanol/water in dodecane) droplet in two-dimensional configuration is simulated. Grid independency has been checked for both the two-miscible-component and three-component emulsified droplet cases. Depending on the water volume fraction in the sub-droplet, which varies from 10% to 70% and is the key parameter herein, both one and two breakups of the parent dodecane droplet are observed. The characteristics of the sub-droplet "invasion" towards the inside of the parent dodecane droplet are investigated, together with the puffing statistics on the puffing delay time, satellite droplet size, surface areas of both the sub- and parent droplets, and oscillation dynamics of the sub-droplet.

KEY WORDS: *Microexplosion, Puffing, Interface Capturing, Miscible, Emulsified, Emulsion, Multicomponent, Droplet*

*This is the Author Accepted Manuscript, under a Green Open Access agreement, for https://doi.org/10.1615/atomizspr.2024051640.

1. INTRODUCTION

Liquid fuels are first atomised into fine droplets by a spraying process and then mix with air in the combustion chamber of aerospace/automotive engines and gas turbines. The study of the evaporation and combustion characteristics of individual droplets at high temperature is thus important for spray combustion, for present-day transportation and power generation using alternative zero-carbon and carbon-neutral liquid fuels.

Microexplosion and puffing during droplet combustion were first discovered by Ivanov and Nefedov (1965) when studying emulsified droplet combustion. Microexplosion has also been observed in miscible multicomponent droplets (Shang et al., 2020; Wang et al., 1984). Puffing occurs due to a large difference in boiling points between the components of the droplet. Bubbles nucleate and grow in the superheated lower boiling point region inside the droplet, eventually producing puffing or droplet rupture due to the pressure difference between the two sides of the stretched liquid film overwhelmingly dominant over the surface tension. Droplet puffing is of scientific significance since it facilitates the secondary fragmentation and atomisation of sprayed droplets in engineering applications. It has therefore attracted great attention and has been extensively studied (Avulapati et al., 2019; Mikami et al., 1998; Wang et al., 1984). In the past, microexplosion and puffing were mainly studied using a single fibre-suspended droplet (Gan and Qiao, 2011) and free-falling droplets (Han et al., 2017) experimentally.

Computational studies on puffing of a miscible multicomponent droplet used the Rayleigh's growth model to solve the growth of a single, quasi-steady state, symmetric bubble at the centre of the droplet (Zeng and Lee, 2007). The simplified one-dimensional approach has contributed to useful insights into microexplosion using the order-of-magnitude analysis. Similar recent efforts include modelling puffing and microexplosion of a miscible multicomponent (Narasu and Gutheil, 2023) and emulsion (Sazhin et al., 2022) droplet.

To understand puffing and its interaction with the ambient gas in multidimensional space, numerical techniques have been developed with the continuous development of computing power. In Fostiropoulos et al. (2021), a model for the breakup time (or puffing/microexplosion delay) was developed and calibrated by two-dimensional axisymmetric computational fluid dynamics using Navier-Stokes and volume-of-fluid. Volume of fluid was used to predict the secondary breakup, accompanied by puffing, of a two-miscible-component heavy-fuel-oil droplet exposed at high temperatures and low pressures under microgravity conditions in Guida et al. (2022). The puffing of a two-component emulsion droplet was studied by Shinjo et al. (2014) by directly resolving the gas-liquid interfaces, including those between the oil droplet and the ambient gas, between the water satellite-droplet and evaporated water vapour, and between the oil droplet and the water vapour. Puffing dynamics of the emulsion droplet in quiescent air was analysed, showing the possibility of controlling puffing by tuning the parameters of the water droplet and nucleation bubbles. Later a heating model for an emulsion droplet under convection conditions was proposed (Shinjo et al., 2016b), which made it possible to study microexplosion and puffing of an emulsion droplet under convective heating (Shinjo et al., 2016a).

Although the potential of puffing and microexplosion is fully recognised, optimising and controlling the complex multicomponent droplet dynamics is still far from achieved, even whether microexplosion will occur under typical operating conditions of various engineering applications is in question. For instance, it was reported that microexplosion of methanol-in-diesel emulsion droplets under typical high-temperature, high-pressure engine conditions was not observed (Ghosh and Ravikrishna, 2022), while microexplosion was confirmed to have been observed, in high frequencies, both in single droplet burning and spray flame experiments of flame spray

pyrolysis (Stodt et al., 2022).

It is clear that more research is needed to better understand and predict the puffing of a multicomponent droplet, especially favourable conditions for puffing and microexplosion to occur, so optimising and controlling the disruptive droplet dynamics will become possible. In this paper, puffing of a two-miscible-component ethanol/water droplet is first studied by high-fidelity interface-capturing simulation. With the capacity of the code extended to cope with a multicomponent liquid mixture and its phase change, the puffing of an emulsified three-component, ethanol/water in dodecane, droplet is then simulated and investigated. Although two-dimensional configurations have been used in the present study due to computational cost, a numerical framework is now available to study complex multicomponent, either miscible or immiscible (emulsified), droplet dynamics, including puffing and microexplosion.

2. METHODOLOGY

2.1 Mathematical formulations and numerical procedures

The governing equations (Shinjo et al., 2014)

$$\dot{\mathsf{f}} + (\mathbf{u}\cdot\boldsymbol{\nabla})\mathsf{f} = \mathsf{g} \tag{1}$$

are solved for $\mathsf{f} = (\rho, \mathbf{u}, T, Y_i)$, where ρ, $\mathbf{u}$, T, Y_i denote density (kg·m^{-3}), velocity (m·s^{-1}), temperature (K), and the mass fraction (-) of the i-th species, respectively. $\dot{\mathsf{f}} = \partial\mathsf{f}/\partial t$ and

$$\mathsf{g} = (-\rho\boldsymbol{\nabla}\cdot\mathbf{u} + S_\rho, -\rho^{-1}\boldsymbol{\nabla}p + \mathbf{Q}_\mathbf{u} + \mathbf{S}_\mathbf{u}, -\rho^{-1}c_\mathrm{v}^{-1}P_\mathrm{TH}\boldsymbol{\nabla}\cdot\mathbf{u} + Q_T + S_T, Q_{Y_i} + S_{Y_i}), \tag{2}$$

where $P_\mathrm{TH} = T(\partial p/\partial T)_\rho$. For an ideal gas, $P_\mathrm{TH} = p$. $\mathbf{Q}_\mathbf{u}$ includes the viscous and surface tension terms. Q_T includes the work by viscous forces and heat conduction modelled by Fourier's law. Q_{Y_i} is the mass diffusion term modelled by Fick's law.

The level set method in combination with a VOF (Volume of Fluid) method MARS (Multi-interface Advection and Reconstruction Solver) (Kunugi et al., 2001; Sussman and Puckett, 2000) is used to capture interfaces (Shinjo and Umemura, 2010). Surface tension solved by CSF (Continuum Surface Force) method is included in $\mathbf{Q}_\mathbf{u}$ (Brackbill et al., 1992).

Boiling can be modelled using jump conditions at the boiling interface, including

$$h_\mathrm{l}\dot{\omega} = \langle\lambda\boldsymbol{\nabla}T\cdot\mathbf{n}\rangle\,, \tag{3}$$

$$\dot{\omega}\langle Y_i\rangle = -\langle\rho\mathcal{D}\boldsymbol{\nabla}Y_i\cdot\mathbf{n}\rangle \tag{4}$$

for heat and mass transfer (Tanguy et al., 2007). The angle bracket $\langle\cdot\rangle$ denotes the difference of a variable f between the liquid and gas phases at the interface, i.e. $\langle f\rangle = f_\mathrm{L} - f_\mathrm{G}$. h_l is the latent heat of the mixture (J·kg^{-1}). $\dot{\omega}$ denotes the mass rate of evaporation (kg·s^{-1}). λ and $\mathcal{D}$ represent thermal conductivity (W·m^{-1}·K^{-1}) and mass diffusion coefficient (m^2·s^{-1}), respectively. $\mathbf{n}$ is the surface normal unit vector. The subscripts L and G denote liquid and gas, respectively.

The boiling source terms are

$$S_\rho = \rho(\rho_\mathrm{G}^{-1} - \rho_\mathrm{L}^{-1})\dot{\omega}\delta\,, \tag{5}$$

$$\mathbf{S}_\mathbf{u} = \rho^{-1}(\rho_\mathrm{G}^{-1} - \rho_\mathrm{L}^{-1})\dot{\omega}\delta\mathbf{n}\,, \tag{6}$$

$$S_T = -\rho^{-1}c_\mathrm{p}^{-1}h_\mathrm{l}\dot{\omega}\delta\,, \tag{7}$$

$$S_{Y_i} = \rho^{-1}\langle Y_i\rangle\dot{\omega}\delta\,, \tag{8}$$

where δ is the delta function to identify a surface.

The CIP (Cubic Interpolated Pseudo-particle or Constrained Interpolation Profile) method is used to solve the equations in the advection phase. In the non-advective phase, the equation is solved by CCUP (CIP-combined and unified procedure) method. Then in the final acoustic phase, a Poisson equation is solved to obtain the pressure. The detailed method can be found in Shinjo et al. (2014); Takewaki et al. (1985); Yabe et al. (2001).

Unlike mono-component liquid, the concentrations of the gas and liquid components at an interface are no longer equal due to the different boiling points of each component, when phase change occurs in miscible multicomponent liquid. A jump of the mass fractions of the components occurs at the gas-liquid interface. The concentration of a gas component at the gas-liquid interface is strongly dependent on that of the liquid counterpart. In this study, the bubble surface is considered to be in thermodynamic equilibrium, and the relation between the gas and liquid components at the interface can be modelled by phase equilibrium, as

$$X_{i,\mathrm{s}} = \lambda_i X_{i,\mathrm{L}} \frac{p_{i,\mathrm{vap}}}{p} \ , \tag{9}$$

where λ_i (-) is the activity coefficient of a liquid component i. $X_{i,\mathrm{s}}$ and $X_{i,\mathrm{L}}$ denote the mole fractions of component i in the saturated gas and liquid at the interface, respectively. $p_{i,\mathrm{vap}}$ is the vapour pressure of component i.

When $\lambda_i = 1$, the mixture is ideal, satisfying Raoul's law. However, many liquid fuel mixtures, especially those containing hydrogen bonds, differ significantly from an ideal mixture. Thus, in this study, the UNIFAC [UNIQUAC (**uni**versal **qua**si**c**hemical) Functional-group Activity Coefficients] method (Fredenslund et al., 1975) was used to calculate the activity factor λ_i, which has been widely used and can accurately reflect the activities of liquid components (Banerjee, 2013; Narasu et al., 2020; Yang et al., 2021). Considering computational cost and the mixtures under investigation, the calculated mixture phase equilibrium curves determined by UNIFAC are tabulated.

The physical properties of a two-component liquid mixture also vary with the concentrations of the components. In this study they were calculated with reference to Ra and Reitz (2009), using a linear mixing rule based on either mole fractions for the mixture's viscosity and thermal conductivity or mass fractions for its density ($1/\rho$), specific heat at constant pressure and latent heat of evaporation.

2.2 Code validation

The code MicroEXplosion (MEX) (Shinjo and Umemura, 2010, 2011, 2013; Shinjo et al., 2014, 2016a,b; Tanimoto and Shinjo, 2019) is used and has been further developed for this work. MEX has demonstrated its ability to directly simulate boiling surface dynamics (Stefan problem) and linear/nonlinear droplet oscillations (Shinjo et al., 2014), which are directly related to bubble swelling and puffing. In addition, the code can now directly simulate convective heat/mass transfer both in an emulsion (immiscible) and miscible multicomponent droplet, including the fluid dynamics within the droplet, which is essential to simulate puffing dynamics.

The capability of MEX has been demonstrated in studies revealing the microexplosion and puffing dynamics of a two-immiscible-component water-in-oil droplet (Shinjo et al., 2014). To validate further development of the code for two-miscible-component liquid, a bubble was placed in a uniformly superheated liquid and the growth of the bubble is determined. The composition and thermo-physical properties of the ethanol/water liquid pool are listed in Table 1.

Gas parameters are calculated using the ideal gas law. The results in Fig. 1(a) show that the bubble radius growth is overall proportional to $\sqrt{t}$, which is in good agreement with theory. The growth of the bubble is oscillatory with time, which was also observed in Shinjo et al. (2014). The natural oscillation frequency ω_{N} of an isothermal bubble surrounded by a homogeneous liquid can be predicted according to the equation:

$$\omega_{\mathrm{N}} = \sqrt{\frac{3\Delta p + 4\sigma/R_{\mathrm{b0}}}{\rho_{\mathrm{L}} R_{\mathrm{b0}}^2}}\ , \tag{10}$$

where R_{b0} is the equilibrium bubble diameter. Although Eq. 10 was derived for non-growing bubbles, it can be used to estimate the oscillation frequency of growing bubbles. Δp is the initial pressure difference, which is $\sim$ 50,000 Pa. According to the first cycle (I) the equilibrium radius $R_{\mathrm{b0}} \approx 2.2$ μm, the oscillation period $T = 2\pi/\omega_{\mathrm{N}} \approx 0.87$ μs is obtained according to equation (11), which is very close to the duration of the first oscillation cycle of the simulated bubble. The method is used to obtain the subsequent oscillation periods of 1.22 μs (II), 1.68 μs (III) and 2.14 μs (IV), respectively, all of which are very close to the simulation results.

TABLE 1: Composition and thermo-physical properties of the ethanol/water liquid pool. The liquid temperature is T_{l} = 410 K. The pressure is p = 5.0 atm.

	H_2O	C_2H_5OH
Mass fraction Y (-)	0.5	0.5
Density ρ (kg·m^{-3})	850	750
Latent heat h (kJ·kg^{-1})	2,256	850.51
Thermal conductivity λ (W·m^{-1}·K^{-1})	0.68	0.16
Surface tension coefficient σ ($\times 10^{-3}$ N·m^{-1})	47.5	9.9
Viscosity μ ($\times 10^{-4}$ Pa·s)	1.7	2.3

At the same superheating degree $\Delta\theta_0$, a multicomponent bubble grows more slowly than a mono-component one. Figure 1(b) presents the comparisons of the bubble growth constant C_1 among the theoretical, experimental and simulation data, where $C_1 = C_2/\Delta\theta_0 = R_{\mathrm{b}}/\sqrt{t}/\Delta\theta_0$. A binary mixture of *n*-butanol and water is considered. The figure shows the variation of the ratio of the bubble growth constant of the mixture $C_{1,\mathrm{m}}$ to that of water $C_{1,\mathrm{H_2O}}$ with the mass fraction of *n*-butanol. It can be seen that the simulated results agree well with the theoretical and experimental data.

2.3 Case setup

2.3.1 Two-miscible-component ethanol/water droplet

During droplet evaporation, volatile components evaporate faster due to their lower boiling points. In the mixture of water and ethanol studied in this paper, ethanol is the volatile component. This makes non-volatile components gradually accumulate on the droplet surface, and a boundary layer of non-volatile components forms on the droplet surface (Shaw, 1990). The boiling point within the layer is significantly higher than in the region near the centre of the

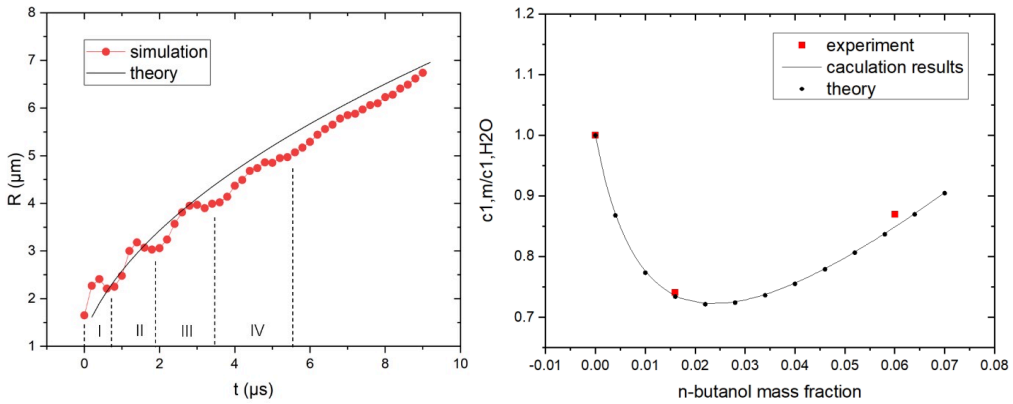

(a) Comparison between simulated and theoretical (Van Stralen, 1968a,b) bubble growth. The initial bubble radius is 1.5 μm.

(b) Bubble growth constant (Van Stralen, 1968a,b).

FIG. 1: Validation.

droplet, which is the fundamental reason for the formation of a superheated lower boiling point region within the droplet. Bubbles nucleate and grow in the superheated region, producing puffing or droplet rupture under the impact of surface tension. Considering that the time scale of the evaporation process is much larger than that of puffing (Shinjo et al., 2014), evaporation is not simulated, and the distribution of components within the droplet is determined by the data in literature (Shaw, 1990). The following simplifications were therefore made. The thickness of the non-volatile component layer is set to be $d_{\mathrm{c}} = 7\% D_{\mathrm{d}}$. The mass fraction $Y_{\mathrm{H_2O}}$ of the non-volatile component (water) in the layer was set to be 1. The droplet diameter D_{d} was set to be 30 μm, which is a typical size for sprayed droplets. Bubble nucleation is not simulated. The initial diameter of the bubble (D_{b}) was set to be 2.6 μm. Figure 2 shows a schematic diagram of the initial conditions. The droplet and air temperatures were set to be T_{d}, and the temperature inside the bubble was the local boiling point. A 381×381 grid with a minimum size of 0.26 μm was used (Shaw, 1990; Tanimoto and Shinjo, 2019). Grid convergence has been checked (see Sec. 3.1.1). The key physical parameters are given in Table 2. The temperature T_{d} 420 K for Cases 1–5 is set up according to the boiling point of ethanol/water mixtures, which is within the range of 398.93–425.55 K.

2.3.2 Three-component ethanol/water-in-dodecane emulsified droplet

Figure 3 and Table 3 show the setup of a three-component ethanol/water-in-dodecane emulsified droplet. The corresponding mass fractions of water in the sub-droplet for Cases E3c-1, E3c-2, E3c-3 and E3c-4 are $Y_{\mathrm{H_2O}} = 14.8\%$ (10 vol.%), 40.2% (30 vol.%), 61% (50 vol.%) and 78.5% (70 vol.%), respectively. The prefix "E3c" indicates an emulsified three-component droplet. For all cases, the superheating degree is set to 50 K. The ambient pressure is $P = 2.0$ bar. See Table 4 for thermo-physical properties of the three components. The properties of a mixture of ethanol and water are determined by the method descried in Sec. 2.3.1. Constant liquid properties have been used due to the short time scale of microexplosion and limited temperature variation. Since the timescale of microexplosion is far shorter than that of heat transfer inside the droplet,

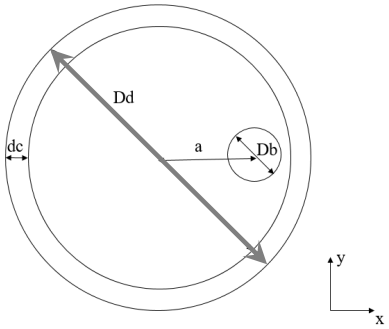

FIG. 2: Setup of the two-miscible-component droplet, nucleation bubble and non-volatile component layer.

Case	$2a/D_\mathrm{d}$	T_d (K)
1	0.596	420
2	0.632	420
3	0.667	420
4	0.702	420
5	0.737	420
6	0.737	415
7	0.737	412.5
8	0.737	411
9	0.737	410

TABLE 2: Droplet and bubble parameters. $D_\mathrm{d} = 30$ μm; $D_\mathrm{b} = 2.6$ μm; $d_\mathrm{c} = 7\%D_\mathrm{d}$ (see Fig. 2).

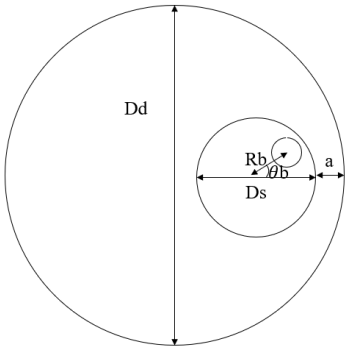

FIG. 3: Setup of the three-component emulsified droplet: A sub-droplet with two miscible components, i.e. ethanol and water, is embedded in the parent dodecane droplet. A nucleation bubble is away from the sub-droplet centre by R_b.

Case	$\varphi_{\mathrm{H_2O}}$
E3c-1	10%
E3c-2	30%
E3c-3	50%
E3c-4	70%

TABLE 3: Case setup. $\varphi_{\mathrm{H_2O}}$: water volume fraction of the ethanol/water sub-droplet. $D_\mathrm{d} = 30$ μm; $D_\mathrm{b} = 2.6$ μm; $a = 6\%D_\mathrm{d}$ (see Fig. 3).

temperature variation of the ethanol/water sub-droplet is confined in a thin layer at the sub-droplet surface, and the variation can be neglected. For other parts of the droplet, the temperature stays at the initial temperature, and therefore the viscosities remains unchanged. In addition, even at the gas-liquid interface layer, temperature change is limited. Therefore, the microexplosion dynamics is not affected significantly by the variation of liquid properties (e.g. viscosities). For gas phases, the physical properties are determined by NIST databases. The initial velocity is 0 everywhere. Since the evaporation timescale of dodecane $C_{12}H_{26}$ is far longer than that of the microexplosion, the effects of dodecane evaporation on puffing and fuel/air mixing under puffing are secondary and therefore neglected. According to Lasheas et al. (1985), a vapour bubble forms due to nucleation. The size of the initial nucleation bubble (< 0.01 μm) is small compared to that of the ethanol/water sub-droplet. In addition, due to surface tension, the internal vapour pressure is high (~ 100 atm). It is known that the first stage in which the growth of a nucleation bubble towards a small bubble is governed by inertia, and the timescale is short (~ 0.1 μm). The high pressure inside the bubble decreases rapidly with the growth of the bubble. The bubble growth

in the next stage is controlled by isobaric diffusion. Resolving the first stage is not attempted in this study due to the requirement for resolution in space and time. The simulations in this study all start with a bubble whose initial size is set to be $0.087D_{\mathrm{d}}$. The impact of the size of the initial bubble on puffing has been checked. If a bigger initial bubble is used, the puffing dynamics is similar, and the earlier growth of the bubble will be excluded. In order to include sufficient details on bubble growth and a more complete process of droplet puffing, this initial droplet diameter is chosen.

TABLE 4: Thermo-physical properties of the three components of the ethanol/water-in-dodecane emulsified droplet. $h_{\mathrm{C_{12}H_{26}}}$ is irrelevant since dodecane evaporation is neglected.

	H_2O	C_2H_5OH	$C_{12}H_{26}$
Density ρ (kg·m^{-3})	944.7	602.8	626.8
Latent heat h (kJ·kg^{-1})	2,256	850.51	-
Thermal conductivity λ (W·m^{-1}·K^{-1})	0.68	0.16	0.1
Surface tension coefficient σ ($\times 10^{-3}$ N·m^{-1})	47.5	9.9	10
Heat capacity c (kJ·kg^{-1}·K^{-1})	4.2	3.35	3.2

3. RESULTS AND DISCUSSION

3.1 Puffing of a two-miscible-component ethanol/water droplet

3.1.1 Grid independency

Three grids, 165×165, 381×381 and 757×757, were tested. The relationship between vapour area metrics and grid resolution of Case 5 was calculated. The vapour area is defined as the area of gas with less than 1% oxygen in mass fraction, which can quantitatively reflect the process from bubble growth to breakage, after which oxygen starts mixing with the boiled vapour through diffusion, causing S to decrease. As shown in Fig. 4(a), the two different grids 381×381 and 757×757 produce similar results, while the 165×165 grid shows unacceptable deviations from the finer-grid results. Therefore, 381×381 was chosen, as in Shinjo et al. (2014); Tanimoto and Shinjo (2019).

3.1.2 Puffing dynamics

The simulated puffing dynamics of Case 5 is shown in Fig. 5. Firstly, the bubble rapidly grows and violently pushes the liquid near the bubble to move away from the centre. Under this impact, the surrounding liquid is deformed, and the bubble expands toward the thinnest part of the liquid around the bubble surface, as shown in Fig. 5(a). The bubble then breaks through by overcoming surface tension in the thin liquid film to eject a satellite-droplet and boiled vapour in Fig. 5(b). At the same time, the liquid indicated by the arrows at the upper and lower parts of the bubble surface continues to expand under the impact of the inertia and boiled vapour. In Fig. 5(c), the liquid on the top and bottom parts is incorporated into the droplet body and drives the local liquid to leave. Protrusion formed on the right side of the main droplet by recoil, as shown in Fig. 5(d), 5(e) and 5(f).

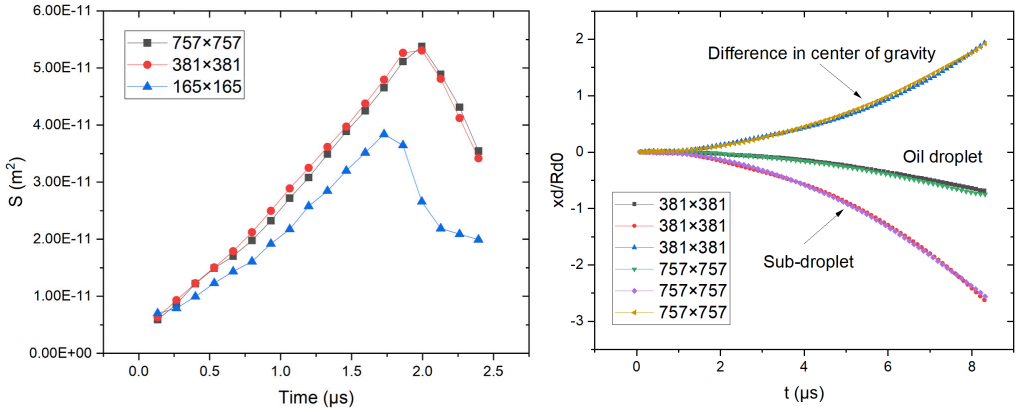

(a) Case 5 in Tab. 2: vapour area S.

(b) Case E3c-4 in Tab. 3: x-coordinate of centre of mass.

FIG. 4: Grid independency check.

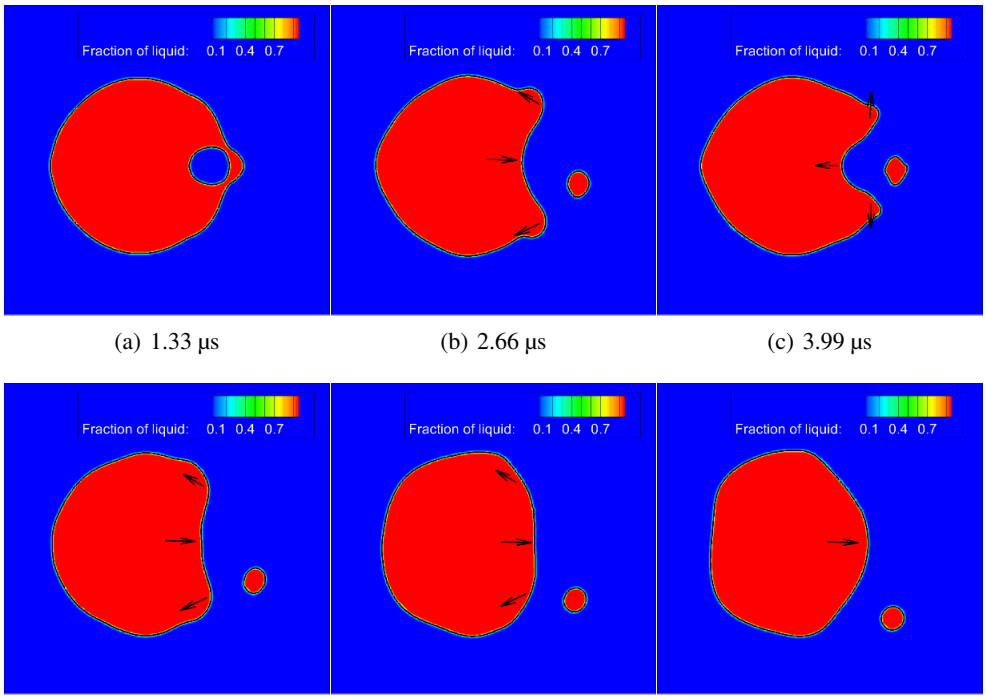

(a) 1.33 μs (b) 2.66 μs (c) 3.99 μs

(d) 5.32 μs (e) 6.65 μs (f) 7.89 μs

FIG. 5: Puffing of Case 5.

Comparing Fig. 5 with the localised puffing observed by high-speed camera (Miglani and Basu, 2015), many similar features can be found, including the outward motion of the liquid on both sides after the bubble rupture and the eventual integration into the droplet body. The

generation of a satellite-droplet and the final droplet bulge were also experimentally observed. Similar to Miglani and Basu (2015), puffing also occurs in three stages: bubble growth, cavity expansion and recoil projection.

The initial droplet diameter in the simulation is 30 μm, which is much smaller than the experimental 2 mm. The experimental microexplosion time scales are < 1 ms for all cases. The simulation shows the microexplosion timescale is < 10 μs. The ratios of the timescale and droplet diameter between the simulation and measurement (100 vs 67.7) are on the same order of magnitude, which may suggest a scaling law can be obtained for droplet microexplosion.

3.1.3 Puffing-enhanced fuel/air mixing

The mass fraction distribution of the gas components after the puffing is shown in Fig. 6. Overall, the boiled vapour generated by puffing was deflected by the satellite-droplet during the outward ejection. Closer to the boiling interface, the higher $Y_{C_2H_5OH}$ and Y_{H_2O}, the lower Y_{O_2}. At $x = 0.4D_d$, the mass fractions of the three components are nearly equal, showing effective mixing. $Y_{C_2H_5OH}$ in the ejected vapour was much higher than Y_{H_2O} near the boiling surface. This is due to the phase equilibrium of the two-component liquid. The lower-boiling-point ethanol is released from inside the droplet by puffing, benefiting the ignition and combustion.

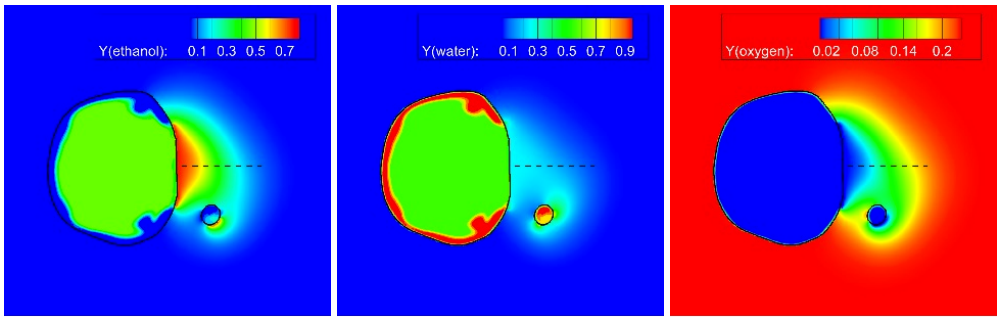

(a) $Y_{C_2H_5OH}$ (b) Y_{H_2O} (c) Y_{O_2}

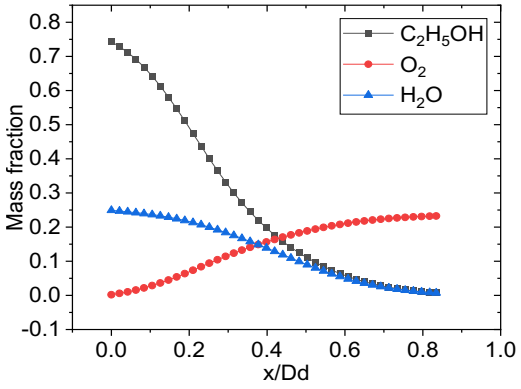

(d) along the dashed line

FIG. 6: Mass fraction distributions of Case 5 at 6.65 μs.

The morphological changes of the droplet during the puffing include the formation of the

satellite-droplet, allowing the boiling surface to be in full contact with air, which will promote vapour/air mixing, as similarly observed in emulsion droplet puffing (Tanimoto and Shinjo, 2019). In order to measure the mixing of vapour/air, the scalar dissipation rate (SDR) χ is used (Shinjo et al., 2016a): $\chi = 2\mathcal{D}|\boldsymbol{\nabla} Y_i|^2$. The SDR distribution of O_2 is shown in Fig. 7. Strong mixing occurs in the two gap regions between the satellite and parent droplets at 3.325 µs after bubble rupture. The change in droplet morphology brings the boiling surface into closer contact with air, which results in the highest SDR at these locations, such as near the satellite-droplet and on the upper and lower sides of the boiling surface of the main droplet. As the puffing proceeds, vapour diffuses into a larger area at 5.985 µs. The SDR at the vapour/air interface is significantly reduced, while the SDR near the boiling surface still remains at high magnitudes ($> 52{,}000\ \mathrm{s}^{-1}$).

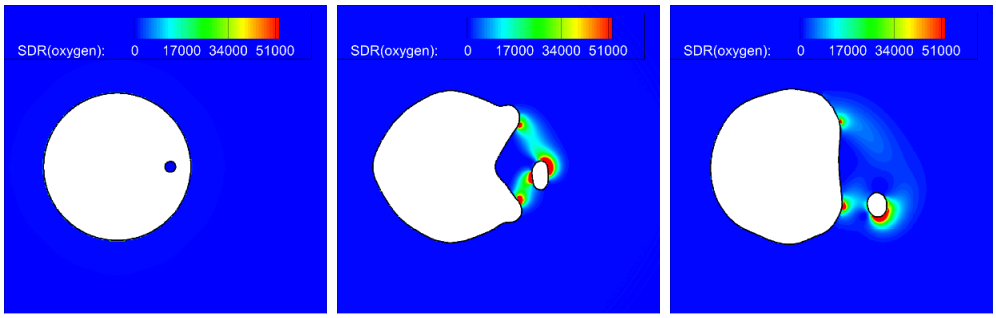

(a) 0.133 µs (b) 3.325 µs (c) 5.985 µs

FIG. 7: SDR (s^{-1}) distribution of O_2 of Case 5.

3.1.4 Breakage time (puffing delay) and satellite-droplet characteristics

It is of great interest to study the effects of the bubble location on puffing, which not only facilitates a better understanding of the puffing dynamics, but also sheds light on a possible way to control and exploit the puffing phenomenon to improve atomisation. Due to the presence of dissolved gases or impurities in actual spray droplets, the degree of superheating for bubble nucleation is difficult to predict (Zeng and Lee, 2007). Therefore, the effect of the initial droplet temperature on puffing has also been studied.

Puffing has great potential for secondary atomisation by generating satellite droplets in much reduced diameters quickly. The variations of the bubble breakage time and the diameter of the generated satellite-droplet (D_s) with the initial position (a) of the bubble and droplet temperature (T_d) are shown in Fig. 8. The further the initial position of the bubble is away from the droplet surface, the longer it takes for puffing to occur and the more adjacent liquid it pushes, thus tending to produce lager satellite droplets. As T_d decreases, the bubble breakage time shows an exponential increase. Decreasing T_d also has a significant effect on droplet fragmentation pattern. When T_d drops to 412.5 K, satellite droplets are no longer generated. Note the satellite droplet size D_s is similar between 415 and 420 K but not identical, with the equivalent diameter being 1.912 and 1.903 µm, respectively. Comparing Fig. 8(a) and 8(b), it is clear that the nucleation bubble depth "a" has a bigger impact on D_s than T_d. For the two cases with different T_d's but an identical nucleation-bubble depth "a", since the growing vapour bubble pushes a liquid "wall" with an identical thickness, which can be quantified by "a", the resultant sub-droplets are on similar size.

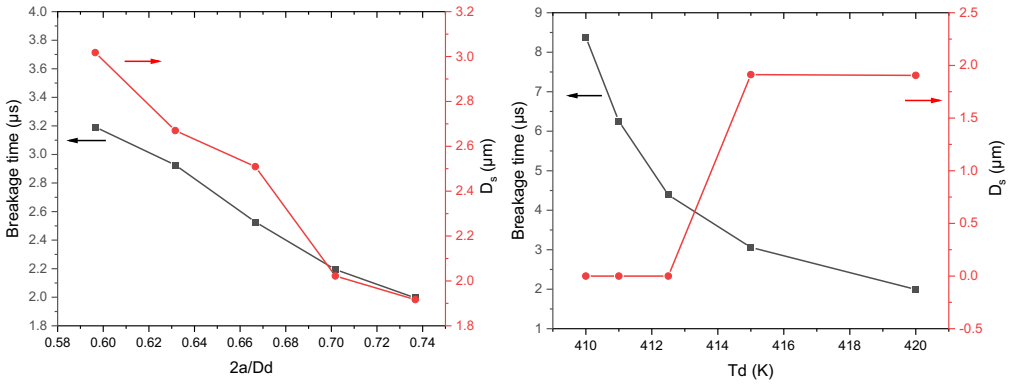

(a) Case 1 → 5: $a \nearrow \Longleftrightarrow$ nucleation → droplet surface

(b) Case 5 → 9: $T_{\mathrm{d}} \searrow$

FIG. 8: Bubble breakage time (puffing delay) and satellite-droplet size (D_{s}).

To better understand the change of the shape of the generated satellite-droplet, a shape factor $\Delta y_{\max}/\Delta x_{\max}$ of the satellite-droplets is determined by $\Delta y_{\max}/\Delta x_{\max} = [\max(y) - \min(y)]/[\max(x) - \min(x)]$, where the coordinate (x, y) is taken from within the satellite droplet, i.e. $(x, y) \in S_{\mathrm{satellite-droplet}}$. Figure 9 shows that $\Delta y_{\max}/\Delta x_{\max}$ reaches 2.5-3.0 at the time of satellite-droplet generation, showing a clear film structure along the direction perpendicular to the bubble push. After the satellite-droplet is separated from the parent, it rapidly recovers to a circular spherical shape under its own surface tension. $\Delta y_{\max}/\Delta x_{\max}$ therefore also shows a gradual decrease and drops to 1.25 at 8 μs, which is already close to 1.0 for a circle. $\Delta y_{\max}/\Delta x_{\max}$ oscillates and the oscillation decays with time. It was caused by the rotation of the satellite-droplet after the detachment. The droplet rotation is mainly due to the unbalanced pulling of the adjacent liquid during the generation of the satellite-droplet. The recovery of the shape of the satellite-droplet and its rotation were also observed in experiments (Miglani and Basu, 2015).

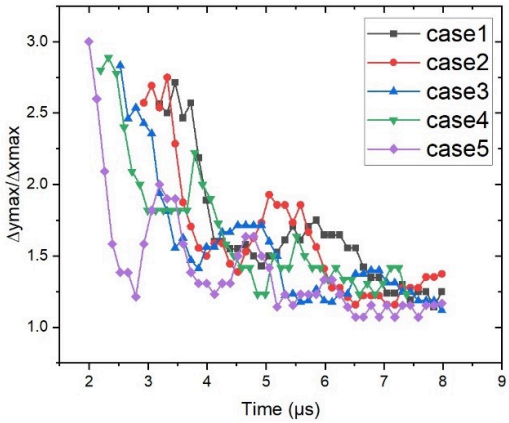

FIG. 9: Satellite-droplet shape variation.

3.1.5 Surface area and boiling mass transfer rate

In addition to generating satellite-droplets to accelerate atomisation, puffing also helps to increase the rate of evaporation through boiling, thereby providing more quickly combustible fuel vapour for burning.

The time histories of the boiling, remaining and total surface areas are shown in Fig. 10(a) and 10(c), where the boiling area + the remaining area = the total area. They were all non-dimensionalised by the initial remaining area (S_0). Since evaporation is much slower than boiling and its effect on the droplet breaking process is minimal, it is not considered. So, the remaining area can also be considered as the evaporation area of a droplet in an actual spray. In Fig. 10(a) and 10(c), all cases show a similar trend in boiling/remaining/total surface areas.

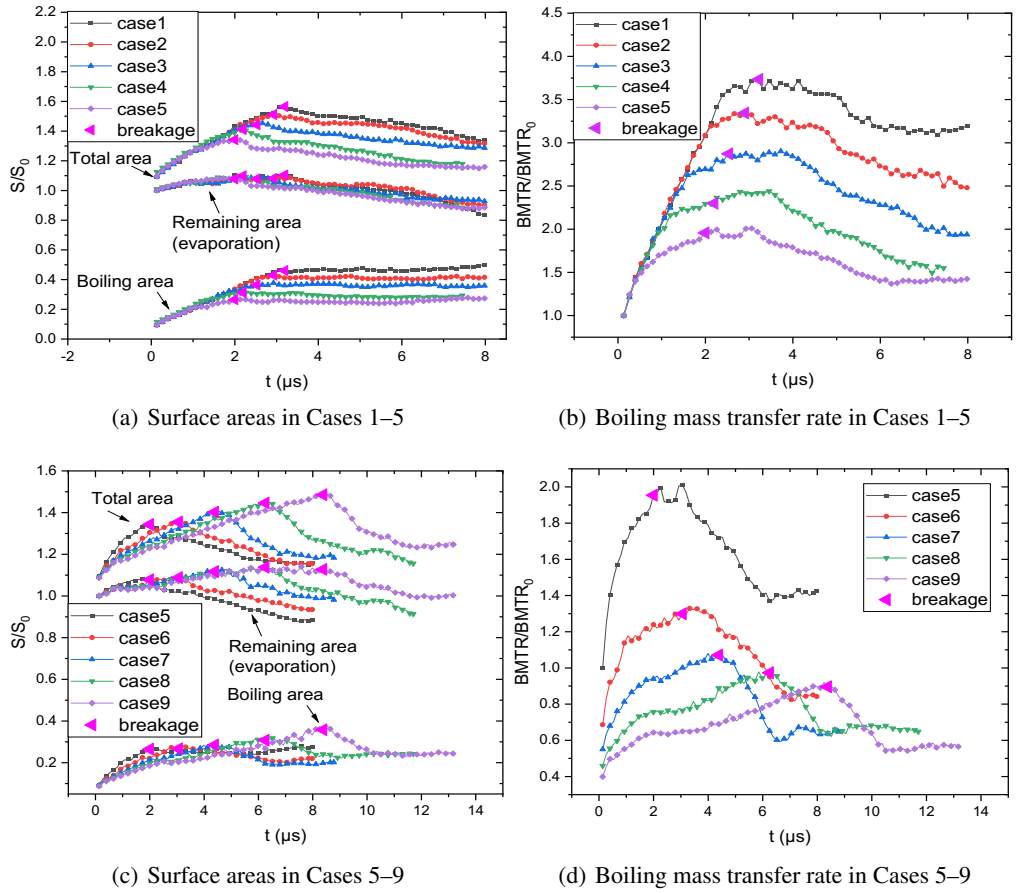

(a) Surface areas in Cases 1–5

(b) Boiling mass transfer rate in Cases 1–5

(c) Surface areas in Cases 5–9

(d) Boiling mass transfer rate in Cases 5–9

FIG. 10: Time history of boiling/remaining/total surface areas and BMTR. From Case 1 to 5, the nucleation bubble moves away from the droplet centre ($a \nearrow$); From Case 5 to 9, the system temperature decreases (see Tab. 2).

For boiling surface area, it first undergoes a bubble growth stage and increases rapidly. Bubble breakage is a turning point. The boiling area stays essentially the same once the bubble is broken. By comparing cases 1-5, the further the initial position of the bubble is away from

the droplet surface, the higher the final stable boiling area. The boiling area of Case 5 finally stabilised at ~ 0.47, which is as much as 1.96 times that of Case 1 (0.24).

For the remaining surface area, the variation is relatively small. The evaporation area gradually increases from 1.0 to ~ 1.1 before the bubble breaks. This is mainly due to the growing bubble pushing adjacent liquid, causing the entire droplet to expand outward. After bubble breakage, the remaining area began to diminish, which is solely responsible for the reduction of the total surface area.

Comparing cases 5-9, the lower the droplet temperature, the slower the growth rate of the boiling area before bubble breakage. However, due to the increase of the bubble breakage time, the maximum boiling/remaining/total areas showed an increasing trend. Unlike cases 1-5, cases 6-9 showed a significant decrease in boiling area after bubble breakage.

The variation of the boiling mass transfer rate (BMTR) is shown in Fig. 10(b) and 10(d). BMTR is non-dimensionalised by its initial value of Case 5 (BMTR_0). Since the evaporative transfer rate is low, BMTR can reflect the mass transfer of the droplet to the surrounding air during puffing. The BMTRs of cases 1-5 all increase with time initially, followed by a decreasing trend, as shown in Fig. 10(b). Similar to the boiling area, an increase in bubble depth (a in Fig. 2) results in a higher BMTR. This is mainly due to the increase in boiling area. However, unlike the boiling area, the BMTR shows a clear downward trend after bubble breakage. Although the boiling area remains unchanged, the presence of the higher-boiling-point boundary layer and the diffusion of temperature in the liquid reduces the temperature difference, which reduces the mass transfer rate per unit boiling area. The drop in droplet temperature causes significant decreases of BMTR during puffing, as shown in Fig. 10(d). The decrease in temperature not only decreases the initial BMTR ($t = 0$) but also inhibits the rise in BMTR during bubble growth. In addition, as the temperature decreases, the puffing experiences a longer time. This means that the temperature diffusion time is longer and has a greater effect on the BMTR per unit area. It is also detrimental to the BMTR.

3.2 Puffing of an emulsified three-component (ethanol/water in dodecane) droplet

3.2.1 Grid independency

Two grids, i.e. 381×381 and 757×757, have been used to run Case E3c-4. The displacements of the centre of mass (COM) of the sub- and parent droplets and their distance are given in Fig. 4(b). The data have been normalised by the initial radius $R_{\mathrm{d0}} = D_{\mathrm{d0}}/2$ of the parent dodecane droplet. As shown, the two grids shown almost overlapping profiles for the three quantities. Therefore, the 381×381 grid has been used for all the cases listed in Tab. 3.

3.2.2 Puffing and after-puffing dynamics

The puffing and after-puffing of the three-component emulsified droplet of Case E3c-4, where water:ethanol=7:3 in vol.% in the sub-droplet, is shown in Fig. 11. In the figure, solid lines are used to indicate gas/liquid and liquid/liquid interfaces. For liquid phases, ethanol/water and dodecane are coloured in red and orange, respectively. Contour plots are used to show the mass fraction, $Y_{\mathrm{H_2O}}$, of water vapour.

As shown, the initial bubble grows rapidly due to boiling. Since the dodecane "film" on the droplet periphery is thin, the film breaks up quickly. The boiled vapour is ejected and a satellite droplet is generated. After the puffing, the boiling surface continues to produce water and ethanol

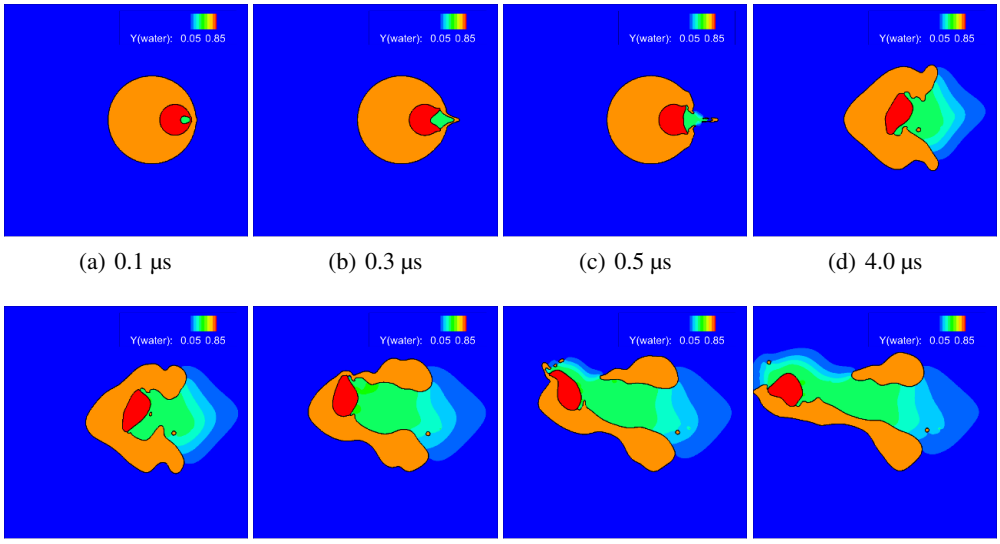

(a) 0.1 μs (b) 0.3 μs (c) 0.5 μs (d) 4.0 μs

(e) 5.0 μs (f) 7.0 μs (g) 8.0 μs (h) 9.0 μs

FIG. 11: Puffing of Case E3c-4, where water:ethanol=7:3 in vol.% in the sub-droplet (coloured in red), with two breakups.

vapour, keeping pushing the ethanol/water sub-droplet towards the inside of the parent dodecane droplet. At the two intersections of the boiling surface and the (inert) interface between dodecane and the gas phase, interfaces deform due to the Landau-Darrieus instability, causing the gradual detachment of the ethanol/water sub-droplet from the parent dodecane droplet due to intense boiling. The boiling surface also undergoes intense oscillation due to the simultaneous effects of pulling and thrust due to the ejecting vapour after the puffing occurs. From Fig. 11, it can be seen that the two effects compete fiercely, and the curvature of the boiling surface decreases initially, which benefits the "invasion" of the ethanol/water sub-droplet towards the inside of the parent dodecane droplet. The puffing vapour is with a high momentum, due to which the invasion of the sub-droplet is fast. This also leads to the second rupture of the parent droplet on its other end, also generating satellite droplets [see Fig. 11(g) and 11(h)].

For Case E3c-2, where the water volume fraction φ_{H_2O} is decreased to 30% in the sub-droplet, the puffing and after-puffing of the three-component emulsified droplet is shown in Fig. 12. Compared to Case E3c-4, when the ejecting vapour contains more ethanol, the speed of the satellite dodecane droplet decreases, as well as the invasion speed of the ethanol/water sub-droplet. The weakening of both the pulling and thrust due to the ejecting vapour has led to no further rupture of the parent dodecane droplet on its other end, which occurs in Case E3c-4, as shown in Fig. 11. It is clear that puffing effects on the secondary breakup of the dodecane droplet can be adjusted or "tuned " via the compositions of ethanol and water in the two-miscible-component sub-droplet.

Overall, the edge regression and sub-droplet detachment are similar to what we have observed before (Shinjo et al., 2014). It is known that the mass flux on a boiling surface will induce the Landau-Darrieus instability, increasing the oscillation of the boiling surface, leading to high vorticity which further boosts the development of the instability, even if the liquid motion is

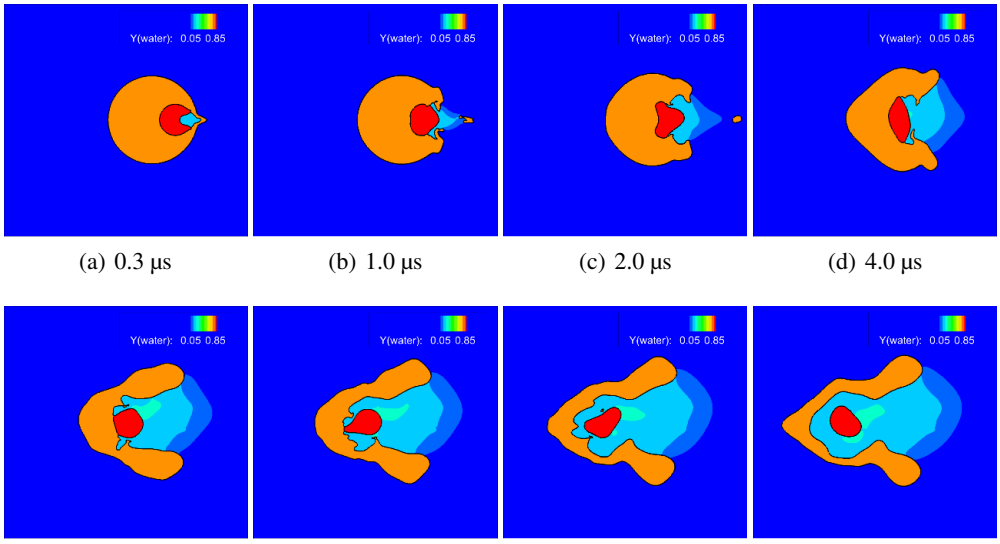

(a) 0.3 μs (b) 1.0 μs (c) 2.0 μs (d) 4.0 μs

(e) 6.0 μs (f) 7.0 μs (g) 8.0 μs (h) 9.0 μs

FIG. 12: Puffing of Case E3c-2, where water:ethanol=3:7 in vol.% in the sub-droplet (coloured in red), with one breakup up to 9 μs.

irrotational. Especially in narrow flow paths formed during and after the puffing, high vorticity regions will be seen. Comparing Case E3c-2 ($\varphi_{C_2H_5OH} = 70\%$) with E3c-4 ($\varphi_{C_2H_5OH} = 30\%$), more ethanol vapour is produced in the former case. However, the mass flux of the boiled vapour is lower, leading to the weakening of the vorticity magnitudes when the puffing occurs as compared to Case E3c-4 (not shown). On the other hand, effects of a slower boiling evaporation on vorticity magnitudes are not significant at later times (not shown). Although a lower mass flux of the boiler vapour will weaken the development of the Landau-Darrieus instability, which does not benefit the detachment of the sub-droplet from the parent one, it will also suppress the puffing vapour's thrust effects on the sub-droplet, leading to a slower invasion of the sub-droplet towards the inside of the parent and thus benefiting the development of the Landau-Darrieus instability. Overall, the ethanol/water sub-droplet is detached from the parent dodecane droplet before the second breakup occurs in Case E3c-2, as shown in Fig. 12.

3.2.3 Ethanol/water sub-droplet "invasion"

In order to measure the impact of the volume fraction of water φ_{H_2O} in the sub-droplet on puffing-induced breakup of the dodecane droplet, the x-coordinates of the centre of mass of the sub- and parent droplets are given in Fig. 13. In Fig. 13(a), the left and right ordinates are the x-coordinates of the ethanol/water sub-droplet x_s and the dodecane parent droplet x_d, respectively, both normalised by the initial radius R_{d0} of the dodecane droplet. It can be seen that both the sub- and parent droplets move towards the left due to the thrust on the sub-droplet and subsequently the invasive pushing of the sub-droplet on the parent droplet. The sub-droplet moves much faster than the parent, indicating a continuous "invasion" of the sub-droplet inwards. With an increase of the volume fraction φ_{H_2O} of water in the sub-droplet, x_d does not vary

significantly. For all cases, the displacement of x_{d} is $\sim 0.6R_{\mathrm{d0}}$ at $t = 8$ µs. On the other hand, the displacement of x_{s} is affected more significantly as $\varphi_{\mathrm{H_2O}}$ increases. At $t = 8$ µs, x_{s} increases from $1.1R_{\mathrm{d0}}$ to $2.62R_{\mathrm{d0}}$ as $\varphi_{\mathrm{H_2O}}$ increases from 10% to 70%, demonstrating the average speed of the sub-droplet COM increases by 138.2%. To better compare the invasion among cases, the relative displacement of the two COMs $x_{\mathrm{d}} - x_{\mathrm{s}}$ is shown in Fig. 13(b). It can be seen that as $\varphi_{\mathrm{H_2O}}$ increases from 10% to 70%, $x_{\mathrm{d}} - x_{\mathrm{s}}$ increases from $0.50R_{\mathrm{d0}}$ to $1.94R_{\mathrm{d0}}$, indicating the average invasion speed increases by 288%. Therefore, an increase of the volume fraction of water in the sub-droplet can enhance the capability of the sub-droplet's inward invasion, and thus the capability of further rupturing the parent dodecane droplet after the first puffing, as the comparison between Figs. 11 and 12 has already revealed.

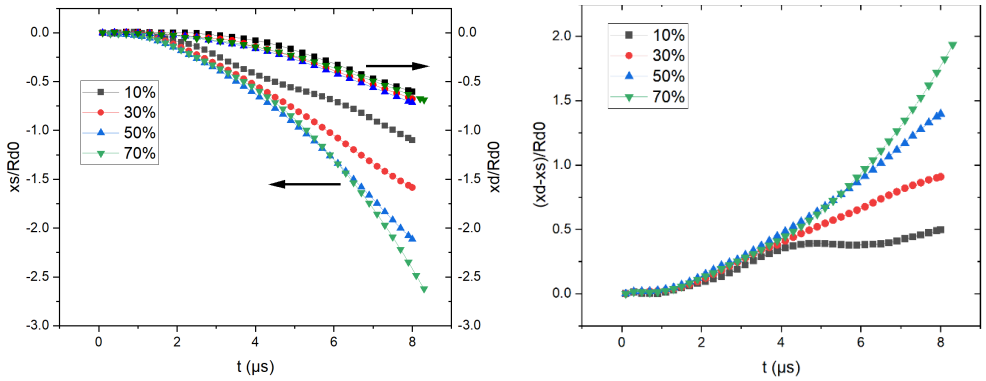

(a) x-coordinates of centre of mass of sub- (x_{s}) and parent (x_{d}) droplets

(b) Distance between COMs of sub- and parent droplets

FIG. 13: Impact of water volume fraction $\varphi_{\mathrm{H_2O}}$ in sub-droplet on its inward invasion.

In addition, the invasion mode changes with $\varphi_{\mathrm{H_2O}}$. At $\varphi_{\mathrm{H_2O}}$ = 10%, the relative displacement $x_{\mathrm{d}} - x_{\mathrm{s}}$ shows a three-stage, increasing-stabilising-increasing, profile; While at $\varphi_{\mathrm{H_2O}}$ = 30% and 50%, $x_{\mathrm{d}} - x_{\mathrm{s}}$ steadily increases; And at $\varphi_{\mathrm{H_2O}}$ = 70%, $x_{\mathrm{d}} - x_{\mathrm{s}}$ increases elliptically, indicating the invasion of the sub-droplet is accelerating due to the stronger thrust produced by boiled vapour, as shown in Fig. 11. As a lower $\varphi_{\mathrm{H_2O}}$, a slower edge detachment of the inert gas/dodecane interface from the boiling gas/ethanol-water interface due to the Landau-Darrieus instability slows the sub-droplet invasion, transforming the invasion speed from a steadily growing mode to a three-stage increasing one.

3.2.4 Puffing statistics

The size of the secondary, satellite droplet produced by puffing is determined by the characteristics of the nucleation bubble, also affecting the puffing delay time. Figure 14 shows the variations of the puffing delay τ_{puff} and the (equivalent) diameter D_{sate} of the satellite droplet with the water volume fraction $\varphi_{\mathrm{H_2O}}$ in the sub-droplet. As $\varphi_{\mathrm{H_2O}}$ increases, the bubble grows more rapidly, the ejecting momentum increases, and the puffing delay decreases. τ_{puff} is 0.7, 0.48, 0.43 and 0.4 µs at $\varphi_{\mathrm{H_2O}}$ = 10%, 30%, 50% and 70%, respectively. Compared to $\varphi_{\mathrm{H_2O}}$ = 10%, the puffing delay at $\varphi_{\mathrm{H_2O}}$ = 70% is shortened by close to half. In addition, with a higher puffing momentum and thus a stronger "pushing" leading to the breakup of the dodecane film on the parent-droplet periphery, the size of the satellite droplet decreases. D_{sate} = 2.90, 2.88, 2.68

and 2.48 μm at φ_{H_2O} = 10%, 30%, 50% and 70%, respectively. Compared to φ_{H_2O} = 10%, the size of the satellite droplet produced by the puffing decreases by 14.48%.

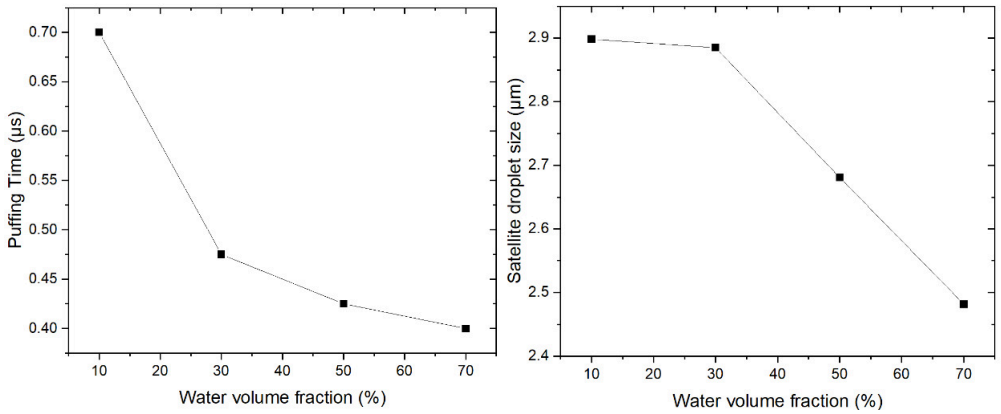

(a) Puffing delay time (b) Satellite droplet size

FIG. 14: Impact of water volume fraction φ_{H_2O} in sub-droplet on puffing delay τ_{puff} and satellite-droplet size D_{sate}.

After the puffing, a large portion of the ethanol/water sub-droplet is still attached to the parent dodecane droplet. The continuous boiled vapour ejection produces a thrust, partly determining the after-puffing dynamics. In this stage, the boiling surface area shows an increasing trend together with oscillation, on which the composition of the sub-droplet has a determining role. Figure 15(a) shows the boiling surface area S_b of the sub-droplet, normalised by the initial surface area S_{d0} of the parent droplet. It can be seen that at φ_{H_2O} = 30% and 50%, S_b shows a three-stage step-increasing trend, i.e., initially an increasing profile before ∼1.8 μs, followed by a decreasing trend in 1.8 − 3.4 μs and finally increasing again after 3.4 μs, indicating the three stages of edge regression, remerging of the boiling ethanol/water and inert dodecane surfaces by shape oscillation and edge regression. At φ_{H_2O} = 10% and 70%, S_b shows a different trend. At φ_{H_2O} = 10%, S_b reaches a much smaller magnitude < 0.15, compared to the other cases in which $S_b \approx 0.2$, stabilises in a much shorter period 1.8 – 2.1 μs, and then increases with oscillations. Therefore, the competing thrust exerted by the puffing vapour on the sub-droplet and edge regression due to the combining Landau-Darrieus/Reyleigh-Taylor instabilities are comparable. At φ_{H_2O} = 70%, S_b shows a similar profile to φ_{H_2O} = 30% and 50% before 3.4 μs, but increases until 5.2 μs, then decreases until 7.1 μs, and finally increases again. The decrease of S_b during 5.2 and 7.1 μs implies that the remerging of the boiling and inert surfaces dominates again.

To quantify the detachment of the sub-droplet from the parent droplet, the ratio of the boiling surface area S_b to the total surface area S_s of the sub-droplet is shown in Fig. 15(c). The ethanol/water sub-droplet is completely detached from the parent droplet if $S_b/S_s = 1$. The profiles of S_b/S_s in Fig. 15(c) appear similar to those of S_b/S_{d0} in Fig. 15(a), implying the total surface area S_s of the sub-droplet does not vary significantly. At 8 μs, S_b/S_s approaches 1 for φ_{H_2O} = 10%, 30% and 50%. When the water volume fraction φ_{H_2O} of the sub-droplet is 70%, only half of the sub-droplet is detached from the parent droplet, i.e., $S_b/S_s \approx 0.55$, at 8 μs.

The profiles of the inert parent-dodecane-droplet surface area S_d, normalised by its initial value S_{d0}, are shown in Fig. 15(b). It can be seen that the droplet shape varies significantly due

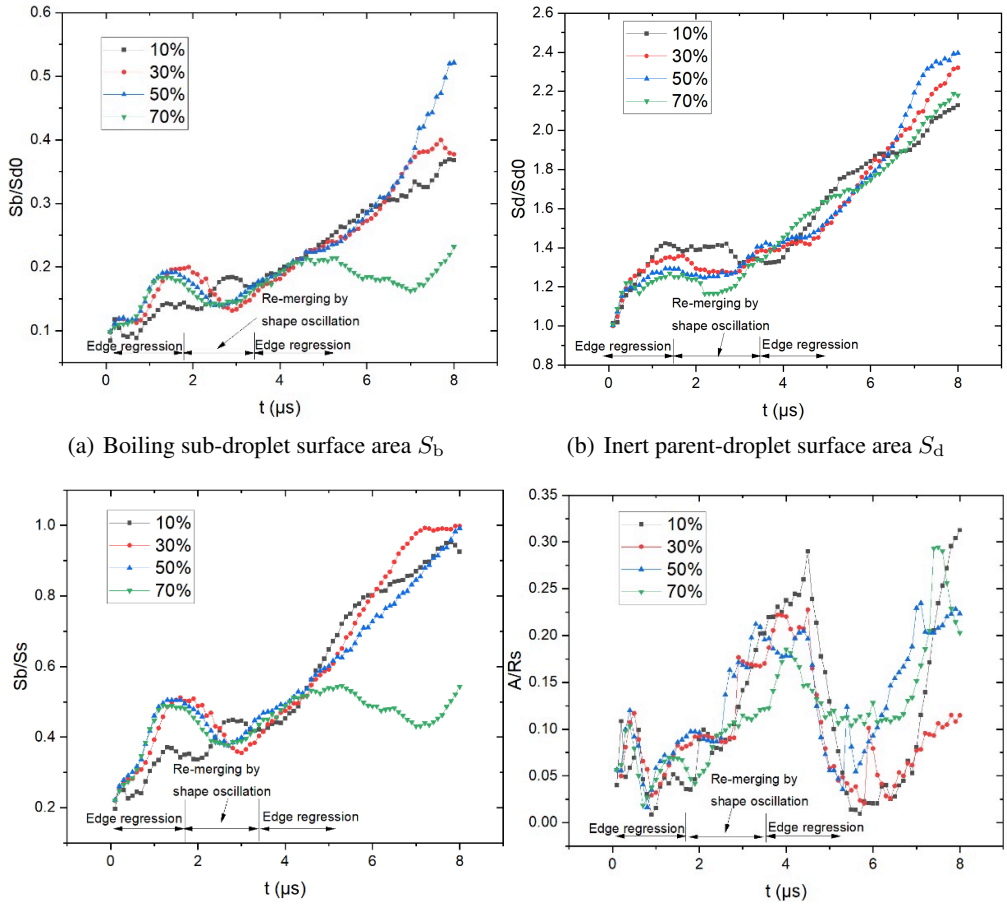

(a) Boiling sub-droplet surface area S_b (b) Inert parent-droplet surface area S_d

(c) Percentage of boiling surface area in sub-droplet (d) Maximum oscillation magnitude of sub-droplet

FIG. 15: Impact of water volume fraction $\varphi_{\mathrm{H_2O}}$ in sub-droplet on sub- and parent droplet statistics.

to the puffing, leading to a rapid increase of the inert-surface area. All cases show a similar increasing trend.

In order to better understand the effects of the oscillating deformation of the sub-droplet on the puffing, the maximal oscillation magnitude A, normalised by the radius of the sub-droplet, is shown in Fig. 15(d). A is obtained by $A = \max_i |R_i - R_\mathrm{s}|$, where R_i is the distance between the i-th identified point on the boiling surface and the centre of mass of the sub-droplet, and R_s is the equivalent radius of the sub-droplet. It can be seen that the maximal oscillation A rapidly grows in the initial $0 - 0.5$ μs, mainly due to the rapid growth of the bubble and then puffing. Afterwards A drops quickly towards 0 at 1 μs. At this time the shape of the sub-droplet is close to a circle [see Fig. 12(b) for instance]. Due to the competing pulling and thrust, the sub-droplet will be stretched and deformed mainly in horizontal directions, leading to an increasing A profile of the sub-droplet in $1.0 - 1.8$ μs. The sub-droplet shape oscillation is beneficial for the detachment of the sub-droplet from the parent, which is indicated by the continuous increases of the boiling sub-droplet surface area S_b in Fig. 15(a) and its percentage $S_\mathrm{b}/S_\mathrm{s}$ in the whole

sub-droplet in Fig. 15(c) in the same time period. Therefore, although the maximal oscillation magnitude A is increasing in this period, the edge regression still dominates, as prior to 1.0 μs. After ∼1.8 μs, vertical oscillations take place instead. This shape deformation mode is not beneficial to the detachment of the sub-droplet from the parent droplet. Therefore, the boiling surface of the sub-droplet and the inert surface of the dodecane droplet will remerge. As shown in Fig. 15(a) and 15(b), both S_b and S_d show a decreasing trend until 3.4 μs. Afterwards for cases where $\varphi_{\mathrm{H_2O}}$ = 10%, 30% and 50%, the boiling surface area S_b of the sub-droplet continues to increase, entering the edge regression stage again. For $\varphi_{\mathrm{H_2O}}$ = 70%, S_b decreases first after $t \approx 5$ μs and then increases again from ~ 7 μs. Seen from the maximal oscillation magnitude A, the shape of the sub-droplet does not recover to close to a circle. This is mainly due to the stronger impact of the thrust after the puffing. The sub-droplet is continued to be stretched in vertical directions and the shape cannot recover, which blocks edge regression, and delays the detachment of the sub-droplet from the parent droplet. Therefore, at $t = 8$ μs, the percentage of the boiling surface area of the sub-droplet $S_\mathrm{b}/S_\mathrm{s}$, as shown in Fig. 15(c), is $\sim 55\%$ only, which is far below the values at $\varphi = 10\%$, 30% and 50%. This indicates an increase of the water volume fraction $\varphi_{\mathrm{H_2O}}$ in the sub-droplet leads to a stronger puffing and thrust. The sub-droplet will be kept to be pushed inwards, stay far from circular shape and attach firmly itself to the concave parent-droplet surface. These after-puffing dynamics inhibit edge regression between the sub- and parent droplets, keeping the "pushing" of the sub-droplet on the parent droplet strong, leading to possible further ruptures of the parent dodecane droplet. Meanwhile, a decrease of $\varphi_{\mathrm{H_2O}}$ leads to the decrease of surface tension of the sub-droplet. Therefore, although the thrust due to puffing decreases with the water volume fraction $\varphi_{\mathrm{H_2O}}$, the oscillation magnitude of the sub-droplet tends to increase with the decrease of $\varphi_{\mathrm{H_2O}}$. It can be seen that $A/R_\mathrm{s} \approx 0.29$ for $\varphi_{\mathrm{H_2O}}$ = 10%, which is far higher than 0.185 for $\varphi_{\mathrm{H_2O}}$ = 70% for the first puffing.

4. CONCLUSIONS

The code MEX (Shinjo et al., 2014) has been further developed to study the puffing of a multicomponent, either miscible or immiscible (emulsified), droplet using high-fidelity interface capturing simulations. Validation against theoretical analysis on bubble growth, quantified using bubble radius and bubble growth rate, in a liquid pool was achieved. Grid independent results have been obtained in the present study.

For the two-miscible-component droplet where ethanol : water = 1 : 1 in wt.%, the effects of the initial bubble position and the initial droplet temperature on puffing were evaluated. The puffing dynamics of the droplet and fuel/air mixing enhancement by puffing were analysed. The simulated puffing dynamics of the ethanol/water droplet fully supports experimental observations, which confirmed bubble growth, cavity expansion and recoil projection as the three key stages during puffing. Satellite-droplets form during the cavity expansion stage. More accurately predicted by a non-ideal multicomponent phase equilibrium model UNIFAC that takes into account liquid component activities, the ejected vapour contains much more ethanol than water, which facilitates the transport of the volatile component inside the droplet to the ambient air. The morphological changes of the droplet caused by puffing promote the contact of the boiling surface with air, significantly increasing the local scalar dissipation rate and thus improving fuel/air mixing. The bubble breakage time or puffing delay shows an exponential increase as the initial droplet temperature decreases. The shape of the satellite droplet is far from a circle at the time of bubble breakage and swiftly develops towards a circle due to surface tension. The shape factor oscillates and the oscillation decays with time due to droplet rotation. With the same initial

droplet temperature, the boiling surface area maintains after bubble breakage, regardless of the initial bubble location. On the other hand, the boiling surface area significantly decreases after bubble breakage with the decrease of the initial droplet temperature. The boiling mass transfer rate shows a clear downward trend after bubble breakage, due to the higher-boiling-point boundary layer and heat transfer in the liquid phase.

For the three-component emulsified, ethanol/water in dodecane, droplet, where favourable conditions for puffing and microexplosion should be easier to identify compared to a multi-miscible-component droplet in general, the water volume fraction $\varphi_{\mathrm{H_2O}}$ in the sub-droplet has been chosen to be the key parameter to study. As $\varphi_{\mathrm{H_2O}}$ increases, a more disruptive impact on the parent dodecane droplet was seen, which is due to the fact that the nucleation bubble grows faster at a higher $\varphi_{\mathrm{H_2O}}$, leading to the subsequent stronger thrust on the sub-droplet due to the puffing vapour. The strong thrust suppresses the interaction between the Reyleigh-Taylor and Landau-Darrieus instabilities at the intersections of the boiling sub-droplet and inert dodecane parent-droplet surfaces, and accelerates the inward invasion of the sub-droplet, which may result in a second breakup of the parent dodecane droplet, as the water volume fraction in the sub-droplet increases to 70%. Meanwhile, the surface tension of the sub-droplet decreases as $\varphi_{\mathrm{H_2O}}$ decreases. Although with a weaker thrust, the oscillation of the sub-droplet is stronger.

Both the puffing delay and satellite droplet size decreases with an increase of $\varphi_{\mathrm{H_2O}}$. The statistics on sub-/parent-droplet surface areas and sub-droplet shape oscillation further demonstrate the characteristics of the puffing and after-puffing sub-droplet-invasion dynamics, which is determined by the competition between edge regression and remerging of the boiling and inert surfaces due to sub-droplet shape oscillation. In general, edge regression and surface remerging occurs in turn until the former plays a dominant role in the sub-droplet dynamics. At $\varphi_{\mathrm{H_2O}} = 70\%$ which is the highest water volume fraction studied in this paper, the fast invasion of the sub-droplet keeps the exposed boiling surface area small with multiple remergings. This also leads to a second rupture of the parent dodecane droplet, whereas for the other cases where $\varphi_{\mathrm{H_2O}}$ is lower, the sub-droplet already detaches itself from the parent.

ACKNOWLEDGMENTS

This work was supported by the National Natural Science Foundation of China (52125605), the Fundamental Research Funds for the Central Universities (2022ZFJH004). In addition, this research was funded in part by Research England. A CC BY or equivalent licence is applied to the Author Accepted Manuscript arising from this submission, in accordance with the grant's open access conditions.

DECLARATION OF ORIGINALITY

This article has not been published elsewhere and has not been simultaneously submitted for publication elsewhere. All tables and figures are our original work and no permissions are required.

REFERENCES

Avulapati, M.M., Megaritis, T., Xia, J., and Ganippa, L., Experimental understanding on the dynamics of micro-explosion and puffing in ternary emulsion droplets, *Fuel*, vol. **239**, pp. 1284–1292, 2019.

Banerjee, R., Numerical investigation of evaporation of a single ethanol/iso-octane droplet, *Fuel*, vol. **107**, pp. 724–739, 2013.

Brackbill, J., Kothe, D., and Zemach, C., A continuum method for modeling surface-tension, *J. Comput. Phys.*, vol. **100**, no. 2, pp. 335–354, 1992.

Fostiropoulos, S., Strotos, G., Nikolopoulos, N., and Gavaises, M., A simple model for breakup time prediction of water-heavy fuel oil emulsion droplets, *Int. J. Heat Mass Transf.*, vol. **164**, p. 120581, 2021.

Fredenslund, A., Jones, R., and Prausnitz, J., Group-contribution estimation of activity-coefficients in nonideal liquid-mixtures, *AICHE J.*, vol. **21**, no. 6, pp. 1086–1099, 1975.

Gan, Y. and Qiao, L., Combustion characteristics of fuel droplets with addition of nano and micron-sized aluminum particles, *Combust. Flame*, vol. **158**, no. 2, pp. 354–368, 2011.

Ghosh, A. and Ravikrishna, V, R., Assessment of microexplosion phenomenon of methanol-in-diesel emulsion droplets under engine-like conditions, *Atom. Sprays*, vol. **32**, no. 3, pp. 53–60, 2022.

Guida, P., Ceschin, A., Saxena, S., Im, H.G., and Roberts, W.L., A computational study of thermally induced secondary atomization in multicomponent droplets, *J. Fluid Mech.*, vol. **935**, p. A12, 2022.

Han, K., Chen, H., Yang, B., Ma, X., Song, G., and Li, Y., Experimental investigation on droplet burning characteristics of diesel-benzyl azides blend, *Fuel*, vol. **190**, pp. 32–40, 2017.

Ivanov, V. and Nefedov, P., *Experimental Investigation of the Combustion Process of Natural and Emulsified Liquid Fuels*, NASA technical translation, Published for the National Aeronautics and Space Administration, and the National Science Foundation, 1965.
URL `https://books.google.co.uk/books?id=MiKinQEACAAJ`

Kunugi, T., Satake, S., and Ose, Y., Direct numerical simulation of carbon-dioxide gas absorption caused by turbulent free surface flow, *Int. J. Heat Fluid Flow*, vol. **22**, no. 3, pp. 245–251, 2001, 3rd International Symposium on Turbulence, Heat and Mass Transfer, NAGOYA, JAPAN, APR 03-06, 2000.

Lasheas, J., Yap, L., and Dryer, F., Effect of the ambient pressure on the explosive burning of emulsified and multicomponent fuel droplets, *Symposium (International) on Combustion*, vol. **20**, no. 1, pp. 1761–1772, 1985, twentieth Symposium (International) on Combustion.
URL `https://www.sciencedirect.com/science/article/pii/S0082078485806731`

Miglani, A. and Basu, S., Effect of particle concentration on shape deformation and secondary atomization characteristics of a burning nanotitania dispersion droplet, *J. Heat Transf.-Trans. ASME*, vol. **137**, no. 10, p. 102001, 2015.

Mikami, M., Yagi, T., and Kojima, N., Occurrence probability of microexplosion in droplet combustion of miscible binary fuels, *Twenty-Seventh Symposium (International) on Combustion, vols 1 and 2*, Burgess, A. and Dryer, F. (Eds.), Combustion Institute, 5001 BAUM BLVD, SUITE 635, PITTSBURGH, PA 15213-1851 USA, pp. 1933–1941, 1998, 27th International Symposium on Combustion, UNIV COLORADO, BOULDER, CO, AUG 02-07, 1998.

Narasu, P., Boschmann, S., Poeschko, P., Zhao, F., and Gutheil, E., Modeling and simulation of single ethanol/water droplet evaporation in dry and humid air, *Combust. Sci. Technol.*, vol. **192**, no. 7, SI, pp. 1233–1252, 2020.

Narasu, P. and Gutheil, E., A new model for puffing and micro-explosion of single titanium(iv) isopropoxide/p-xylene precursor solution droplets, *Int. J. Heat Mass Transf.*, vol. **202**, p. 123647, 2023.

Ra, Y. and Reitz, R.D., A vaporization model for discrete multi-component fuel sprays, *Int. J. Multiph. Flow*, vol. **35**, no. 2, pp. 101–117, 2009.

Sazhin, S.S., Shchepakina, E., Sobolev, V.A., Antonov, V, D., and Strizhak, P.A., Puffing/micro-explosion in composite multi-component droplets, *Int. J. Heat Mass Transf.*, vol. **184**, p. 122210, 2022.

Shang, W., Yang, S., Xuan, T., He, Z., and Cao, J., Experimental studies on combustion and microexplosion characteristics of n-alkane droplets, *Energy Fuels*, vol. **34**, no. 12, pp. 16613–16623, 2020.

Shaw, B., Studies of influences of liquid-phase species diffusion on spherically symmetrical combustion of miscible binary droplets, *Combust. Flame*, vol. **81**, no. 3-4, pp. 277–288, 1990.

Shinjo, J. and Umemura, A., Simulation of liquid jet primary breakup: Dynamics of ligament and droplet formation, *Int. J. Multiph. Flow*, vol. **36**, no. 7, pp. 513–532, 2010.

Shinjo, J. and Umemura, A., Detailed simulation of primary atomization mechanisms in diesel jet sprays (isolated identification of liquid jet tip effects), *Proc. Combust. Inst.*, vol. **33**, no. 2, pp. 2089–2097, 2011.

Shinjo, J. and Umemura, A., Droplet/turbulence interaction and early flame kernel development in an autoigniting realistic dense spray, *Proc. Combust. Inst.*, vol. **34**, no. 1, pp. 1553–1560, 2013.

Shinjo, J., Xia, J., Ganippa, L.C., and Megaritis, A., Physics of puffing and microexplosion of emulsion fuel droplets, *Phys. Fluids*, vol. **26**, no. 10, p. 103302, 2014.

Shinjo, J., Xia, J., Ganippa, L.C., and Megaritis, A., Puffing-enhanced fuel/air mixing of an evaporating n-decane/ethanol emulsion droplet and a droplet group under convective heating, *J. Fluid Mech.*, vol. **793**, pp. 444–476, 2016a.

Shinjo, J., Xia, J., Megaritis, A., Ganippa, L.C., and Cracknell, R.F., Modeling temperature distribution inside an emulsion fuel droplet under convective heating: A key to predicting microexplosion and puffing, *Atom. Sprays*, vol. **26**, no. 6, pp. 551–583, 2016b.

Stodt, M.F.B., Groeneveld, J.D., Maedler, L., Kiefer, J., and Fritsching, U., Microexplosions of multicomponent drops in spray flames, *Combust. Flame*, vol. **240**, p. 112043, 2022.

Sussman, M. and Puckett, E., A coupled level set and volume-of-fluid method for computing 3d and axisymmetric incompressible two-phase flows, *J. Comput. Phys.*, vol. **162**, no. 2, pp. 301–337, 2000.

Takewaki, H., Nishiguchi, A., and Yabe, T., Cubic interpolated pseudo-particle method (cip) for solving hyperbolic-type equations, *J. Comput. Phys.*, vol. **61**, no. 2, pp. 261–268, 1985.

Tanguy, S., Menard, T., and Berlemont, A., A level set method for vaporizing two-phase flows, *J. Comput. Phys.*, vol. **221**, no. 2, pp. 837–853, 2007.

Tanimoto, D. and Shinjo, J., Numerical simulation of secondary atomization of an emulsion fuel droplet due to puffing: Dynamics of wall interaction of a sessile droplet and comparison with a free droplet, *Fuel*, vol. **252**, pp. 475–487, 2019.

Van Stralen, S., The growth rate of vapour bubbles in superheated pure liquids and binary mixtures: Part i: Theory, *Int. J. Heat Mass Transf.*, vol. **11**, no. 10, pp. 1467–1489, 1968a.

Van Stralen, S., The growth rate of vapour bubbles in superheated pure liquids and binary mixtures: Part ii: Experimental results, *Int. J. Heat Mass Transf.*, vol. **11**, no. 10, pp. 1491–1512, 1968b.

Wang, C., Liu, X., and Law, C., Combustion and microexplosion of freely falling multicomponent droplets, *Combust. Flame*, vol. **56**, no. 2, pp. 175–197, 1984.

Yabe, T., Xiao, F., and Utsumi, T., The constrained interpolation profile method for multiphase analysis, *J. Comput. Phys.*, vol. **169**, no. 2, pp. 556–593, 2001.

Yang, W., Xia, J., Wang, X.Y., Wan, K.D., Megaritis, A., and Zhao, H., Predicting evaporation dynamics of a multicomponent gasoline/ethanol droplet and spray using non-ideal vapour-liquid equilibrium models, *Int. J. Heat Mass Transf.*, vol. **168**, p. 120876, 2021.

Zeng, Y. and Lee, C.F.F., Modeling droplet breakup processes under micro-explosion conditions, *Proc. Combust. Inst.*, vol. **31**, no. 2, pp. 2185–2193, 2007.